

1 **Length and time scales for precipitation during carbon**
2 **mineralization**

3 **Michael A. Chen¹, Weipeng Yang¹, Huan Peng¹, Peter K. Kang^{1,2}, Vaughan**
4 **R. Voller^{2,3}**

5 ¹Department of Earth and Environmental Sciences, University of Minnesota, Minneapolis, MN, 55455,
6 USA

7 ²St. Anthony Falls Laboratory, University of Minnesota, Minneapolis, MN 55455, USA

8 ³Department of Civil, Environmental, and Geo- Engineering, University of Minnesota, Minneapolis, MN,
9 55455

10 **Key Points:**

- 11 • We develop a first-order carbon mineralization model and perform a scaling anal-
12 ysis to identify key length and time scales
- 13 • Through the scaling analysis, we define expressions for the operational length and
14 shutoff time of a mineralization operation
- 15 • We apply the scaling length to estimate effective first-order precipitation rates and
16 expected shutoff times at a field site

Abstract

This work seeks to identify the key length and time scales associated with CO₂ mineralization in basalt reservoirs. This is achieved through the development and application of a simple yet complete model of the fate and transport of a supersaturated CO₂-charged fluid moving unidirectionally through an initially uniform basalt rock. Assuming a first-order surface precipitation dominates mineralization, the model consists of three coupled equations describing, (i) the spatiotemporal evolution of porosity, hydraulic conductivity, and specific surface area, (ii) the resulting temporal and spatially varying fluid discharge, and (iii) the fate and transport of reactant in the aqueous phase. The model operates until ‘shutoff’ when precipitation-induced pore clogging blocks flow. A dimensional analysis provides length and time scales that characterize the extent and duration of field-scale carbon mineralization. These scales are applied to a field site to estimate poorly constrained mineralization parameters, notably, the effective first-order reaction rate constant.

Plain Language Summary

A promising method to combat global climate change is to sequester carbon dioxide through carbon mineralization. Unlike geologic carbon sequestration, where carbon must remain trapped in aquifers for millennia by an intact caprock, carbon mineralization securely stores carbon by rapidly converting injected carbon dioxide into carbonate rocks. A major challenge in designing these systems, however, is knowing how aquifer properties and injection parameters determine how large a mineralization site must be as well as the time over which it can operate before clogging. Here, we develop a simple model based on the formation of carbonate rocks in a basalt aquifer and analyze it to determine these necessary length and time scales. We find that the length scale of mineralization depends on the injection pressure, aquifer conductivity, and reaction rate of carbonation, while the time scale for shutoff depends on initial porosity, reaction rate, and how efficiently the carbonate minerals can fill the aquifer. We also show, using data from a field-scale carbon mineralization operation, how this scaling can be used to estimate a range of values for an effective reaction rate constant. Together, the modeling and scaling results provide powerful tools for the research and development of carbon mineralization.

1 Introduction

Carbon sequestration technologies have long been considered a primary pathway of mitigating climate change arising from the overabundance of CO₂ gas in our atmosphere. An emerging technology that shows promise is the capture of carbon in the subsurface through the mineralization of CO₂ by injection into mafic (basalts) and ultramafic rock reservoirs (Snæbjörnsdóttir et al., 2017, 2018, 2020; Clark et al., 2020; Kelemen et al., 2020; Power et al., 2013; Matter et al., 2016; White et al., 2020). The advantage of this approach is that it ‘locks’ the carbon into the rock, handily mitigating the risk of CO₂ leaking back into the atmosphere. Conventional approaches (i.e. through geologic storage) in relatively inert aquifers predict mineralization occurs, but only after tens of thousands of years. By contrast, aquifers containing mafic and ultramafic rocks can be dissolved by CO₂, liberating cations that result in precipitation of carbonate rocks in a matter of only a few years. The critical starting point for engineering carbon mineralization is to identify the factors that enhance or limit the ability to precipitate carbonate minerals in subsurface rock masses. This is the first step toward ultimately answering the critical questions: *For a given mineralization process what is the ultimate capacity of carbon that can be stored?* and *How long will it take for this capacity to be realized?*

66 There are two end-member cases to consider in starting to answer these questions.
 67 At one end we might consider using reservoirs of ultramafic rock (e.g., peridotite) which
 68 are highly reactive to carbon mineralization but have very low permeability. Here, the
 69 capacity of the operation will rest on engineering fluid flow by creating and maintain-
 70 ing fluid flow paths (Kelemen et al., 2020). This could be accomplished by leveraging
 71 the mechanical forces unleashed by the expanding mineralization products, known as re-
 72 action driven cracking. At the other end, we might use basalt reservoirs (as in the Carb-
 73 Fix project in Iceland or Wallula Basalt Pilot Project in the United States) where min-
 74 eralization reactions are slower, but permeabilities are large enough to permit flow (Snæbjörnsdóttir
 75 et al., 2018; Callow et al., 2018; Snæbjörnsdóttir et al., 2020; Matter et al., 2016; White
 76 et al., 2020). In this case, which will be our focus here, determining the carbon storage
 77 potential essentially reduces to estimating the length and time scales of a field opera-
 78 tion, in particular:

- 79 1. *The process length scale (i.e. aquifer size) needed to achieve complete mineraliza-*
 80 *tion of carbon from an injected CO₂ laden fluid*
- 81 2. *The process time before the precipitate products ‘clog’ and terminate flow pathways*

82 Our methodology to make these estimates will be through the development of a
 83 model that describes the interacting coupled chemical and transport processes that are
 84 involved, focused on a case where precipitation is the rate limiting process compared to
 85 dissolution. By applying a dimensional scaling analysis to the model, we identify and
 86 extract the relevant length and time scales that control carbon mineralization. We demon-
 87 strate that these length and time scales provide critical and fundamental information for
 88 designing successful carbon mineralization processes in basalt and similar rock masses.

89 2 A Carbon Mineralization Precipitation Model

90 2.1 Overview of Model

91 Towards the aim of determining the carbon mineralization storage potential of a
 92 given reservoir, we will consider a model system where a prescribed constant pressure
 93 head gradient transports CO₂-charged water through a one-dimensional porous reser-
 94 voir of length $0 \leq x \leq L$, see Fig. 1. We consider simplified precipitation reaction cases,
 95 such as $A(\text{aq}) + B(\text{aq}) \rightarrow P(\text{s})$, where an injected reactant A mixes with reactant B in
 96 the aquifer to form a precipitate. In the case of carbon mineralization in mafic or ultra-
 97 mafic rocks, A, B, and P might represent carbonate ions, cations released by the dissolved
 98 host rocks, and precipitated carbonate minerals, respectively. As the precipitate forms
 99 it will decrease the porosity in the reservoir, which in turn decreases the flow, eventu-
 100 ally leading to complete clogging of the reservoir and a flow shutoff. The overall aim of
 101 the model is to identify the length over which mineralization occurs before shutoff ter-
 102 minates the operation. This requires construction of three interacting and coupled model
 103 components:

- 104 1. an expression for the porosity change within the pore spaces as a function of min-
 105 eral precipitation on the pore surfaces, which is driven by the reaction of dissolved
 106 carbonate and cations,
- 107 2. an equation to describe the flow of the fluid through the reservoir, accounting for
 108 changes of porosity in space, and
- 109 3. an equation describing the fate and transport of the aqueous mineralization re-
 110 action reactants, also accounting for changes in porosity in space.

111 In total these components are able to describe and account for the competition between
 112 the flow of the CO₂ charged water and the clogging of the flow pathways.

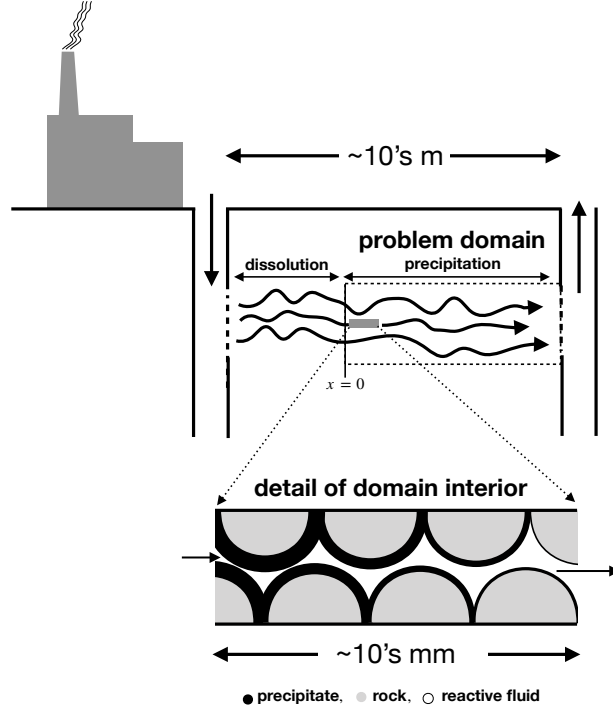


Figure 1. Schematic of a carbon mineralization operation and a representation of the problem domain whose entrance is where precipitation initiates, $x = 0$, and whose exit is at the outflow at $x = L$. This is the porous media reservoir over which precipitation occurs. The model describes the system at the continuum scale, but the schematic provides a view of the pore scale for reference to how precipitation and pore clogging is effectively modeled.

113

2.2 Key Assumptions

114

115

116

117

118

Before we begin to derive our governing equations and relationships, we emphasize that the objective in building our model is to balance between simplicity and reality. We aim to capture the first-order critical features of the system, simplifications that will provide identification of the key process and phenomena controlling the length and time scales. In this light, the key assumptions in our model are the following:

119

120

121

122

123

124

125

126

1. We only consider precipitation in the domain of interest, i.e., dissolution reactions, dissolving the host rock and releasing cations for mineralization, occur upstream of the domain entrance at $x = 0$.
2. The sole reaction that forms the mineral precipitate has unit stoichiometry with pseudo-first-order kinetics.
3. Precipitation occurs only on pore surfaces.
4. To leading order, as precipitation occurs, the hydraulic conductivity and specific surface area are functions of the porosity, i.e.,

127

$$K(x, t) = K_i g_k(\phi(x, t)) \quad (1)$$

128

129

and

$$S(x, t) = S_i g_s(\phi(x, t)), \quad (2)$$

130

131

132

where K_i [m/s] and S_i [m²/m³] are the values of the conductivity and specific surface area at the initial porosity, ϕ_i , and the values of the functions at the initial porosity are $g_k(\phi_i) = g_s(\phi_i) = 1$.

133 5. The flow through the porous medium is governed by Darcy's law where the dis-
 134 charge q [$\text{m}^3/\text{m}^2/\text{s}$] (volume flux per unit cross-sectional area of the porous medium),
 135 is given by

$$136 \quad q(x, t) = \phi u(x, t) = -K(x, t) \frac{\partial h}{\partial x} = -K_i g_k(\phi) \frac{\partial h}{\partial x} \quad (3)$$

137 where $u(x, t)$ [m/s] is the seepage velocity (the fluid velocity in the pore spaces)
 138 and $h(x, t)$ [m] is the pressure head.

139 6. At the initial time, before the reactants are introduced, the porosity ϕ , hydraulic
 140 conductivity K [m/s], and specific surface area S [m^2/m^3] of the porous medium
 141 in the domain take constant values.

142 7. The fluid density and precipitate densities in the porous medium take constant
 143 values where changes in density due to chemical reactions or the dissolution of CO_2
 144 into pore fluids are assumed to be negligible.

145 2.3 Model Components

146 2.3.1 Precipitation Reaction

147 As stated, the rate law for the precipitation reaction is assumed to be pseudo first-
 148 order in the reactant concentration C ,

$$149 \quad r = k^* S_i g_s(\phi) \left(1 - \frac{C}{C_{eq}} \right) = k g_s(\phi) (C_{eq} - C) \quad (4)$$

150 where k^* is the geochemical reaction rate constant [$\text{mol}/\text{m}^2/\text{s}$], C_{eq} the equilibrium con-
 151 centration of the main reactants [mol/m^3], and $k = k^* S_i / C_{eq}$ is the pseudo-first-order
 152 reaction rate constant. The use of pseudo first-order rate laws is a common practice in
 153 the interpretation and modeling of precipitation reactions (Morse et al., 2007; Nancol-
 154 las & Reddy, 1971; Reddy & Nancollas, 1971, 1976; Lasaga, 1997). A geochemical deriva-
 155 tion of this expression from transition state theory, as well as special cases where these
 156 first-order kinetics will readily appear is discussed in the Supporting Information.

157 2.3.2 The Porosity Change

158 The reaction rate in eq.(4) represents the rate at which reactant is consumed per
 159 unit volume of the domain. This rate of consumption will be related in the rate of for-
 160 mation of new solid volume per unit volume of the domain through precipitation, expressed
 161 as the negative rate of the change of porosity $-\frac{\partial \phi}{\partial t}$. Noting our unit stoichiometry, re-
 162 actant mass conservation (i.e. mass of reactant plus the precipitate) gives the relation
 163 between consumption of reactant and rate of increase of volume by the precipitate as

$$164 \quad \frac{\partial \phi}{\partial t} = \nu_S r = \nu_S k g_s(\phi) (C_{eq} - C) \quad (5)$$

165 where ν_S is the molar volume of the precipitate; the appropriate initial condition for this
 166 rate equation is $\phi(x, 0) = \phi_i$.

167 2.3.3 Flow

168 Due to our assumptions of constant, but potentially different densities in the liq-
 169 uid and solid phases, the rate of change in mass, in a fixed control volume, due to the
 170 formation of precipitates is

$$171 \quad \dot{m} = (\rho - \rho_p) \frac{\partial \phi}{\partial t}, \quad (6)$$

172 ρ [kg/m^3] is the liquid density and ρ_p [kg/m^3] is the density of the precipitate. This
 173 mass rate is related to the net rate of flow in and out of the volume, which can be ex-

174 pressed in terms of the divergence of the discharge, i.e.,

$$175 \quad \dot{m} = (\rho - \rho_p) \frac{\partial \phi}{\partial t} = -\rho \frac{\partial q}{\partial x} \quad (7)$$

176 On dividing through by the fluid density ρ , defining the density ratio $\rho_r = \rho_p/\rho$, and
 177 using both Darcy's law [eq.(3)] and the expression for porosity change [eq.(5)], we can
 178 write this balance as the following equation,

$$179 \quad (1 - \rho_r) \nu_S k g_s(\phi) (C_{eq} - C) = \frac{\partial}{\partial x} \left([K_i g_k(\phi)] \frac{\partial h}{\partial x} \right), \quad 0 \leq x \leq L, \quad (8)$$

180 with initial condition $\phi(x, 0) = \phi_i$ and boundary conditions of prescribed heads at the
 181 ends of the domain, i.e., $h(0, t) = h_0 > h(L, t) = h_L$.

182 **2.3.4 Reactant Fate and Transport**

183 We also require an advection-dispersion-reaction model to describe the fate and trans-
 184 port of the reactant, given by

$$185 \quad \frac{\partial(\phi C)}{\partial t} = \frac{\partial}{\partial x} \left([K_i g_k(\phi)] \frac{\partial h}{\partial x} C \right) + \frac{\partial}{\partial x} \left(D \frac{\partial C}{\partial x} \right) \quad (9)$$

$$+ k g_s(\phi) (C_{eq} - C) + \frac{\partial \phi}{\partial t} C, \quad 0 \leq x \leq L,$$

186 with initial condition $C(x, 0) = C_{eq}$ as well as boundary conditions $C(0, t) = C_0$, and
 187 $(\partial C(L, t)/\partial x) = 0$. The first term on the right-hand side of eq.(9) is the contribution
 188 from advective transport. The second term accounts for the contribution of dispersive
 189 transport, where $D = D_L + \phi D_m$ is the dispersion coefficient [m²/s]; D_L is the longi-
 190 tudinal dispersion and D_m is the molecular diffusion. The third term is the rate of con-
 191 sumption of the reactant in forming the precipitate, see eq.(4). The last term accounts
 192 for the loss of fluid mass due to precipitation reducing the pore space. On combining this
 193 last term with the left-hand side, we can rewrite the fate and transport equation as

$$194 \quad \phi \frac{\partial C}{\partial t} = \frac{\partial}{\partial x} \left(K_i g_k(\phi) \frac{\partial h}{\partial x} C \right) + \frac{\partial}{\partial x} \left(D \frac{\partial C}{\partial x} \right) \quad (10)$$

$$+ k g_s(\phi) (C_{eq} - C), \quad 0 \leq x \leq L,$$

195 In further developing this model we will neglect contributions from molecular diffusion
 196 because we should expect this to be orders of magnitude smaller than the longitudinal
 197 dispersion. Thus, following Bear (1972), we can model the dispersion coefficient as

$$198 \quad D = D_L = \alpha_L u = \alpha_L \left(\frac{q}{\phi} \right) \quad (11)$$

199 where α_L [m] is the longitudinal dispersivity. Typically, α_L scales with the domain size
 200 Gelhar et al. (1992), i.e., $\alpha_L = \beta_L L$, a choice that, on using the Darcy expression for
 201 discharge [eq. (3)] and the expression for g_k , generates the following model for the dis-
 202 persion coefficient,

$$203 \quad D = -\beta_L L \frac{K_i g_k(\phi)}{\phi} \frac{\partial h}{\partial x}, \quad (12)$$

204 which assumes that the head gradient is negative. On inserting this treatment into our
 205 fate and transport model [eq.(9)], we arrive at the advection-dispersion-reaction equa-
 206 tion

$$207 \quad \phi \frac{\partial C}{\partial t} = \frac{\partial}{\partial x} \left(K_i g_k(\phi) \frac{\partial h}{\partial x} C - \beta_L L \left[\frac{K_i g_k(\phi)}{\phi} \frac{\partial h}{\partial x} \right] \frac{\partial C}{\partial x} \right) +$$

$$k g_s(\phi) (C_{eq} - C), \quad 0 \leq x \leq L. \quad (13)$$

2.4 A Model of Carbon Mineralization

Gathering the appropriate equations together, the coupled model for carbon mineralization through precipitation is formed as:

Porosity [eq.(5)] :

$$\frac{\partial \phi}{\partial t} = \nu_S k g_s(\phi)(C_{eq} - C),$$

with $\phi(x, 0) = \phi_i$.

Flow [eq.(8)]:

$$(1 - \rho_r) \nu_S k g_s(\phi)(C_{eq} - C) = \frac{\partial}{\partial x} \left(K_i g_k(\phi) \frac{\partial h}{\partial x} \right), \quad 0 \leq x \leq L,$$

with $\phi(x, 0) = \phi_i$, $h(0, t) = h_0$, and $h(L, t) = h_L$.

Reactant fate and transport [eq. (13)]:

$$\phi \frac{\partial C}{\partial t} = \frac{\partial}{\partial x} \left(K_i g_k(\phi) \frac{\partial h}{\partial x} C - \beta_L L \left[\frac{K_i g_k(\phi)}{\phi} \frac{\partial h}{\partial x} \right] \frac{\partial C}{\partial x} \right) + k g_s(\phi)(C_{eq} - C), \quad 0 \leq x \leq L,$$

with $C(x, 0) = C_{eq}$, $C(0, t) = C_0$, and $(\partial C(L, t)/\partial x) = 0$.

2.5 Examples of Constitutive Models

As noted, to solve the coupled model equations [eqs. (5), (8), (13)], we will need to introduce constitutive models for the hydraulic conductivity and specific surface area functions, $g_k(\phi)$ and $g_s(\phi)$, respectively. Here, fully recognizing the existence of alternative choices, we provide a basic example of a constitutive model for each of these variables.

2.5.1 Hydraulic Conductivity

A classical model for the hydraulic conductivity would be Kozeny-Carman, though other models can be used as appropriate (Kozeny, 1927; Sabo & Beckingham, 2021; Carman, 1997). This would set the conductivity function g_k as

$$g_k(\phi) = \frac{\phi^3(1 - \phi_i)^2}{(1 - \phi)^2 \phi_i^3} \quad (14)$$

2.5.2 Specific Surface Area

Experiments and measurements indicate that it is reasonable to expect that specific surface will trend upwards with decreasing porosity (Noiriel et al., 2009; Helgeson et al., 1984). A general representation of this behavior can be captured by setting the specific surface area as

$$g_s(\phi) = \frac{(1 - \phi)^m}{(1 - \phi_i)^m} \quad (15)$$

where $m \geq 0$. Here, to explore the range of possibilities, we will consider two end-members. Setting $m = 1$ results in a linear increase in specific surface area with decreasing porosity, while setting $m = 0$ makes the specific surface area constant with respect to porosity.

3 Dimensional Analysis

For a given domain length L and specified constitutive models for hydraulic conductivity and specific surface area, the solution of the governing equations in section 2.4

244 requires specifying 10 parameters

$$245 \quad [k, \nu_S, C_{eq}, C_0, K_i, \rho_r, h_0, h_L, \beta_L, \phi_i],$$

246 some of which may be difficult to fully characterize. Below we carry out a dimensional
 247 analysis to reduce the number of parameters. This is done in two steps. First through
 248 developing a non-dimensional form of the governing equations, followed by a scaling anal-
 249 ysis that eliminates lower order terms.

250 3.1 Dimensionless Model Equations

251 We propose the following dimensionless scalings for space, time, pressure head, and
 252 reactant concentration

$$253 \quad \xi = \sqrt{\frac{k}{K_i \Delta h}} x, \quad \tau = \nu_S (C_0 - C_{eq}) kt, \quad \eta = \frac{h - h_L}{\Delta h}, \quad \Gamma = \frac{C - C_{eq}}{C_0 - C_{eq}}. \quad (16)$$

254 The choice of length scale captures the competing effects of advective transport and re-
 255 action on the reactant concentration. We can expect that in cases where reaction is very
 256 fast compared to transport that the resulting profiles of flow and concentration will be
 257 compressed, and vice versa, with slow reaction and fast flow stretching concentration pro-
 258 files out. The choice of time scale normalizes time to the initial rate of porosity forma-
 259 tion.

260 With these scalings in hand we can define the following dimensionless parameters:
 261 the dimensionless domain length

$$262 \quad \ell = \sqrt{\frac{k}{K_i \Delta h}} L, \quad (17)$$

263 the dimensionless flow discharge (Darcy Flux)

$$264 \quad \psi = -g_k(\phi) \frac{\partial \eta}{\partial \xi}, \quad (18)$$

265 the yield (the relative volume of the precipitate created by the reaction)

$$266 \quad Y = \nu_S C_0, \quad (19)$$

267 and the initial supersaturation ratio for each component

$$268 \quad R = \frac{C_0}{C_{eq}}. \quad (20)$$

269 Further, on making the substitutions

$$270 \quad x = \sqrt{\frac{K_i \Delta h}{k}} \xi, \quad t = \frac{\tau}{\nu_S k (C_0 - C_{eq})}, \quad h = \eta \Delta h + h_L, \quad (21)$$

$$C = \Gamma (C_0 - C_{eq}) + C_{eq},$$

271 into eqs. (5), (8), and (13), we arrive at the following set of dimensionless equations:

272 Porosity:

$$273 \quad \frac{\partial \phi}{\partial \tau} = -g_s(\phi) \Gamma \quad (22)$$

274 with $\phi(\xi, 0) = \phi_i$.

275 Flow:

$$276 \quad -(1 - \rho_r) Y \left(1 - \frac{1}{R}\right) g_s(\phi) \Gamma = \frac{\partial}{\partial \xi} \left(g_k(\phi) \frac{\partial \eta}{\partial \xi} \right) = -\frac{\partial \psi}{\partial \xi} \quad (23)$$

277 with $\eta(0, \tau) = 1$ and $\eta(\ell, \tau) = 0$.

278 Reactant fate and transport:

279
$$Y\phi \left(1 - \frac{1}{R}\right) \frac{\partial \Gamma}{\partial \tau} = \frac{\partial}{\partial \xi} \left(-\psi \left(\Gamma + \frac{1}{R-1} \right) + \beta_L \ell \left[\frac{\psi}{\phi} \right] \frac{\partial \Gamma}{\partial \xi} \right) - g_s(\phi)\Gamma \quad 0 \leq \xi \leq \ell, \quad (24)$$

280 with $\Gamma(\xi, 0) = 0$, $\Gamma(0, \tau) = 1$, and $\partial \Gamma / \partial \xi(\ell, \tau) = 0$.

281 3.2 Simplified Dimensionless Model

282 The values of the reactant supersaturation and yield are important in understand-
 283 ing the behavior of both the flow and the reactive transport equations. A large value of
 284 R will ensure the efficiency of the operation by providing ample supply of reactants. Here,
 285 our expectation is that $R > 10$, which is discussed further in the Supplementary In-
 286 formation. In terms of determining the yield, we note that the molar volume of the min-
 287 eral precipitate is well constrained and will have a value of $O(10^{-5})$ (Parkhurst & Ap-
 288 pelo, 2013). The value of the initial concentration can be determined from the given in-
 289 jection condition. The field value reported from CarbFix 1 is 840 [mol/m³] which would
 290 provide a value of the yield Y on the order of 0.01 (Snæbjörnsdóttir et al., 2018, 2020).
 291 However, our model uses the *in-situ* concentration at the start of the precipitation, which
 292 we expect may be reduced from the injection value. Thus, it is reasonable to project that
 293 model values of Y will be less than 0.01. In the Supporting Information we further ex-
 294 plore the possible value ranges for the parameters and terms in our dimensionless model.

295 Based on our understanding of the expected size of the yield, $Y < 0.01$, and ini-
 296 tial supersaturation ratio, $R > 10$, we can, using the data values in our SI, make some
 297 simplifications of the governing dimensionless equations for flow and transport. We start
 298 this simplification by noting that:

- 299 1. In our current governing equations the following parameters $(1 - \rho_r)$, $g_s(\phi)$, and
 300 $(1 - 1/R)$ are all order 1.
- 301 2. Expected field values for the porosity and dispersion coefficient are $\phi \sim 0.1$ and
 302 $\beta_L \sim 0.1$ respectively.
- 303 3. Values of the dimensionless domain length are $\ell < 10$; this is confirmed in sub-
 304 sequent analysis.
- 305 4. A representative dimensionless discharge is $\psi \sim \frac{1}{\ell}$, which, based on the expected
 306 domain length above, will take values between 0.1 and 1.
- 307 5. The dimensionless concentration is bounded in $0 < \Gamma \leq 1$, with, due to its de-
 308 creasing value with increasing ξ , an average domain value noticeably less than or-
 309 der 1.

310 In the light of this information, we can conclude that the left-hand side of (23) will
 311 take a value of order 10^{-2} or less, suggesting that it is reasonable to approximate the
 312 dimensionless discharge as divergence free. Further, with reference to eq.(24), we see that
 313 the ratios of the advection to transient terms $(\frac{1}{\ell Y \phi})$ and dispersion to transient terms
 314 $(\frac{\beta_L \ell}{\phi^2 Y})$ will be order 100 or larger. These imply that it is reasonable to neglect the tran-
 315 sient term on the left-hand side of eq.(24). Assuming a divergence-free discharge and drop-
 316 ping the transient term in the transport equations, we arrive at a simplified dimension-
 317 less model for carbon mineralization:

318 Porosity:

319
$$\frac{\partial \phi}{\partial \tau} = -g_s(\phi)\Gamma \quad (25)$$

320 with $\phi(\xi, 0) = \phi_i$ —identical to eq.(22).

321 Flow:

$$322 \quad \frac{\partial}{\partial \xi} \left(g_k(\phi) \frac{\partial \eta}{\partial \xi} \right) = -\frac{\partial \psi}{\partial \xi} = 0 \quad (26)$$

323 with $\eta(0, \tau) = 1$ and $\eta(\ell, \tau) = 0$.

324 Reactant fate and transport:

$$325 \quad -\psi \frac{\partial \Gamma}{\partial \xi} + \beta_L \ell \psi \frac{\partial}{\partial \xi} \left(\frac{1}{\phi} \frac{\partial \Gamma}{\partial \xi} \right) - g_s(\phi) \Gamma = 0 \quad (27)$$

326 with $\Gamma(0, \tau) = 1$, $\Gamma(\xi, \tau) = 0$, $(\partial \Gamma(\ell, \tau) / \partial \xi) = 0$, and the divergence-free flow.

327 Dropping terms that include the yield effectively states the rate of change of porosity is slow enough that its effect on the flow and transport can be neglected. We recognize that dropping these terms may result in some loss of accuracy, in particular when the yield is close to its upper limit of 0.01. However, in the context of our objective here, i.e., identification of the governing length and time scales of mineralization, assuming a divergence-free discharge and dropping the transient term in eq. (24) are reasonable approximations. The key advantage of this step is that after providing appropriate constitutive models for hydraulic conductivity and specific surface area, we only need to specify the initial porosity ϕ_i and dimensionless longitudinal dispersivity β_L —aquifer intrinsic properties—to resolve the model.

337 4 Length and Time Scales for Carbon Mineralization Processes

338 4.1 Process Length

339 The simplified and dimensionless models for transport and flow are pseudo-steady state, changing only with the slowly changing porosity field. The implication is that, at given time τ , if we know the current porosity and surface area profiles, we can solve the steady state equation given in eq. (27) to determine the current concentration profile $\Gamma(\xi, \tau)$. With this in hand, we can approximate an effective length $\ell_m(\tau)$ over which mineralization is occurring by locating the position where $\Gamma(\xi, \tau) = \Gamma_{ex}$, where Γ_{ex} is a small value (e.g., 0.01) that indicates a close to complete depletion of the reactant. We should expect that the point $\ell_m(\tau)$ will migrate backwards in time as the flow slows due to the decrease in porosity. Thus, the furthest extent that reactants will reach, defined as the *process length* ℓ_p , can be determined by solving eq. (27) for the initial $\Gamma(\xi, 0)$ profile. Following some rearrangement, this involved solving the ODE

$$350 \quad \frac{d^2 \Gamma}{d\xi^2} - \left[\frac{\phi_i}{\beta_L \ell_p} \right] \frac{d\Gamma}{d\xi} - \left[\frac{\phi_i}{\beta_L} \right] \Gamma = 0, \quad 0 \leq \xi \leq \ell_p, \quad \Gamma(0) = 1, \quad (d\Gamma(\ell_p) / d\xi) = 0; \quad (28)$$

351 note we are assuming the domain is at the process length ℓ_p and have imposed the initial time values for the constant porosity ϕ_i , $g_s(\phi) = 1$, and discharge $\psi_i = 1/\ell_p$. Equation (28) is a homogenous ODE with constant coefficients. Since, by design $\Gamma(\ell_p, 0) = \Gamma_{ex}$ is small, we can arrive at an accurate approximate solution by replacing the zero gradient condition at $\xi = \ell_p$ with the condition $\Gamma(\xi, \tau) \rightarrow 0$ as $\xi \rightarrow \infty$, giving

$$356 \quad \Gamma(\xi) = \exp(-a\xi); \quad a = \frac{1}{2} \left(\sqrt{\left[\frac{\phi_i}{\beta_L \ell_p} \right]^2 + 4 \left[\frac{\phi_i}{\beta_L} \right]} - \left[\frac{\phi_i}{\beta_L \ell_p} \right] \right). \quad (29)$$

357 This allows us to form the following relationship for the process length

$$358 \quad a\ell_p = |\ln(\Gamma_{ex})|, \quad (30)$$

359 leaving the possibility open to provide alternative settings for the mineralization thresh-
 360 old concentration Γ_{ex} . Between the expression for the constant a in eq. (29) and the re-
 361 lationship in eq. (30), we can explicitly solve for the process length

$$362 \quad \ell_p = \sqrt{|\ln(\Gamma_{ex})| + |\ln(\Gamma_{ex})|^2 \frac{\beta_L}{\phi_i}} \quad (31)$$

363 The value of ℓ_p obtained from the relationship in eq. (31) provides an optimum pro-
 364 cess length scale for a mineralization operation. If the extent of the field is much longer,
 365 then CO_2 will escape the system without mineralizing. In the opposite case, the domain
 366 will not be efficiently used. For $0.001 < \Gamma_{ex} < 0.01$, $0.1 < \phi_i < 0.3$, and $0 < \beta_L <$
 367 0.1 , we can find the range of ℓ_p values as

$$368 \quad 2.1 (\Gamma_{ex} = 0.1, \phi, \beta_L = 0) < \ell_p < 7.4 (\Gamma_{ex} = 0.001, \phi_i = 0.1, \beta_L = 0.1), \quad (32)$$

369 which confirms $\ell < 10$. Values from this range can readily be converted to a dimensional
 370 length scale through eq. (21) giving

$$371 \quad L_p = \ell_p \sqrt{\frac{K_i \Delta h}{k}} \quad (33)$$

372 4.2 Process Time to Shutoff

373 In addition to a characteristic length scale we are also interested in determining
 374 a relevant time scale for shutoff, which indicates the operation time scale. On noting that
 375 shutoff first occurs at $x = 0$, where the reactant concentration is always at its highest
 376 value of $\Gamma = 1$, we can evaluate a shutoff time on direct solution of eq. (25). Using our
 377 generic specific surface area function in eq. (15), the porosity change equation at the en-
 378 trance can be written as

$$379 \quad \frac{\partial \phi}{\partial \tau} = -\frac{(1 - \phi)^m}{(1 - \phi_i)^m}, \quad 0 \leq m \leq 1, \quad (34)$$

380 with $\phi(\xi, 0) = \phi_i$. Defining complete shutoff to occur when we reach zero porosity at
 381 the entrance, i.e., $\phi(\xi = 0, \tau) = 0$, this equation is readily solved for the shutoff time
 382 using separation of variables. On recognizing that the shutoff time decreases monoton-
 383 ically with increasing values of m , we can consider bounding end member solutions of
 384 $m = 0$ or $m = 1$. In the former, the inlet porosity changes at a constant rate giving
 385 $\tau_{m=0} = \phi_i - \phi$. For the latter, $\tau_{m=1} = \log\left(\frac{1-\phi_i}{1-\phi}\right) (\phi_i - 1)$. Solving each expression
 386 for the time when $\phi = 0$ gives

$$387 \quad \tau_{m=0} = \phi_i, \quad \tau_{m=1} = (\phi_i - 1) \log(1 - \phi_i), \quad \tau_{m=0} > \tau_{m=1} \quad (35)$$

388 These two predictions are not much different. When $\phi_i = 0.1$, the linear case time is
 389 0.0948, while the constant case time is 0.1. Since it provides an upper bound on the di-
 390 mensionless time to shutoff, we propose adopting $\tau_{m=0} = \phi_i$ as the dimensionless pro-
 391 cess time scale. Substituting into the time scaling from the non-dimensionalization [eq.
 392 (21)], we obtain

$$393 \quad t_{\text{off}} = \frac{\phi_i}{Yk} \left(\frac{R}{R-1} \right) \approx \frac{\phi_i}{\nu_S C_0 k} \quad (36)$$

394 where we have used the facts that $R > 10$ and $Y = \nu_S C_0$.

395 4.3 Relevant Dimensionless Groups for Carbon Mineralization

396 We can also write out the field length scale in terms of the appropriate Damköhler
 397 numbers, which give the effective scales of reaction and transport relevant to a miner-

398 alization operation. Combining and rearranging eq.(31) and eq.(33) gives

$$399 \quad L_p = \sqrt{|\ln(\Gamma_{ex})| + |\ln(\Gamma_{ex})|^2 \frac{\beta_L}{\phi_i}} \sqrt{\frac{K_i \Delta h}{k}}. \quad (37)$$

400 On noting that, at the initial time, $t = 0$, the dispersion is

$$401 \quad D_i = \beta_L L_p \frac{q}{\phi_i} = \beta_L L_p \frac{K_i \Delta h}{L_p} \frac{1}{\phi_i} = \beta_L \frac{K_i \Delta h}{\phi_i} \quad (38)$$

402 which can be substituted to give

$$403 \quad L_p = \Delta h \sqrt{\frac{|\ln(\Gamma_{ex})|}{\text{Da}_I} + \frac{|\ln(\Gamma_{ex})|^2}{\text{Da}_{II}}} \quad (39)$$

404 where

$$405 \quad \text{Da}_I = \frac{k \Delta h}{K_i} \quad (40)$$

406 is the first Damköhler number, expressing the ratio of reaction rate to advective trans-
407 port rate, and

$$408 \quad \text{Da}_{II} = \frac{k \Delta h^2}{D_i} = \frac{k \Delta h \phi_i}{\beta_L K_i} \quad (41)$$

409 is the second Damköhler number, expressing the ratio of reaction rate to dispersive trans-
410 port rate. Thus, if we can determine the Damköhler numbers for a given field condition
411 and specify the extent of mineralization required—i.e., setting the exit value of Γ_{ex} —
412 we can obtain an estimate of the required process length. This scaling also indicates the
413 main controls on the process length are both the intrinsic characteristics of the aquifers,
414 K_i , ϕ_i , β_L , and k , as well as externally controlled parameters of the operation, Γ_{ex} and
415 Δh . Similarly, analysis of the shutoff times shows that the main extrinsic parameter set-
416 ting shutoff is the injected reactant concentration, C_0 , while the other parameters (ν_s ,
417 ϕ_i , k) are primarily controlled by the aquifer conditions. It is important to note that the
418 value of C_0 is not necessarily the concentration injected at the wellhead because of aquifer
419 geochemistry and mixing of injected waters with the ambient formation waters (Morse
420 et al., 2007; Clark et al., 2020; Gysi & Stefánsson, 2011; Snæbjörnsdóttir et al., 2018).
421 These factors will cause the concentration of reactants when precipitation initiates to
422 vary from the injected values.

423 5 Practical Applications of the Scaling Analysis

424 5.1 Estimates for parameter field values

425 Calculation of L_p and t_{off} requires estimation or determination of a few relevant
426 field parameters beyond the parameters already discussed (i.e. Y , Γ_{ex} , etc.), specifically
427 Δh , K_i , β_L , ϕ_i , and k . Here, we discuss some reasonable values of these parameters as
428 an example of how these time and length scales can be used.

429 The constant head gradient: This is effectively set by the operator and is depen-
430 dent on the pumps used as well as the formation characteristics. In our calculations here,
431 we consider a value of $\Delta h = 100$ m.

432 The dispersion coefficient: The value of β_L is ultimately defined by structure of the
433 formation of itself, but can be characterized with field-testing of the target formation with
434 passive tracer tests. Here, we consider $0 < \beta_L < 0.1$.

435 The initial hydraulic conductivity: Conductivities can vary widely depending on
436 the host rock (i.e. basalt) as well as the properties of the injected fluid after it has mixed
437 with the formation water because of changing temperature, CO_2 concentrations, etc. In

many sites, the presence of fractures will further alter the effective conductivity and relative times of transport, or result in multiple domains with dramatically different conductivities (Viswanathan et al., 2022). Based on reported permeability ranges for vesicular basalts and with water flow, we consider a range of $10^{-7} < K < 10^{-3}$ [m/s] (Saar & Manga, 1999; Clark et al., 2020; Snæbjörnsdóttir et al., 2020). While this is a large range, this can be readily constrained through appropriate aquifer characterization.

The initial porosity: In the aquifers targeted for mineralization, one can expect a range of porosities which can be characterized as a part of site selection. Characterization of the target formation may necessarily wish to also use these to better select functions $g_k(\phi)$ and $g_s(\phi)$ that are appropriate to the site. The porosity is additionally necessary to understand beyond its impact on conductivity since it sets the maximum space where mineralization can occur. Here, we consider $0.1 < \phi_i < 0.3$.

The first-order reaction rate constant: This term has the most uncertainty to it because of uncertainty in the underlying parameters, C_{eq} , k^* , and S_i . While k^* can be determined from *ex-situ* experiments for a single mineral, it is well established that hydrodynamic conditions, mixing, and other dissolved solutes will influence the value of this relevant to *in-situ* conditions (Lasaga, 1995, 1997; Arvidson et al., 2003; Lin & Singer, 2005; Morse et al., 2007; Plummer et al., 1979, 1978; Kang et al., 2019). These factors also do not consider the variable kinetics of the different metal carbonates that may form. Similarly, the value of S_i represents a continuing point of contention for modeling these reactions. Putting aside uncertainties resulting from mineralogical heterogeneity in a target aquifer, there even remain questions whether surface areas should be derived from the geometry of the mineral surface, BET surface area measurements, or some other related parameter, which creates significant variability (Anovitz et al., 2022; Awolayo et al., 2022; Gouze et al., 2003; Gouze & Luquot, 2011; Morse et al., 2007; Helgeson et al., 1984; Noiriél et al., 2009). The combination of these uncertainties result in k being very difficult to constrain *a priori*, but a representative range may be $10^{-8} < k < 10^{-3}$ [1/s].

So to summarize, to our best estimates, we consider the following possible field parameter values and ranges

$$\begin{aligned}
 Y &< 0.01 \\
 0.001 &< \Gamma_{ex} < 0.01 \\
 0 &< \beta_L < 0.1 \\
 \Delta h &= 100 \text{ [m]} \\
 0.1 &< \phi < 0.3 \\
 10^{-7} &< K_i < 10^{-3} \text{ [m/s]} \\
 10^{-8} &< k < 10^{-3} \text{ [1/s]}
 \end{aligned} \tag{42}$$

5.2 Back calculation of reaction rate

The most striking feature of our estimates for field parameters in eq.(42) is the 5 orders magnitude range in the estimate for the reaction rate k and initial conductivity K_i . We saw above that eq. (31) predicts dimensionless process length to be within the relatively constrained values of 2 to 7. When we use these values along with our estimated range of field values in eq.(42) with eq.(37), the resulting dimensional penetration length falls within the range of

$$20 \text{ cm} < L_p < 20 \text{ km}; \tag{43}$$

this range captures what we might expect in the field, but its end values may not be feasible given current reports from mineralization efforts (Clark et al., 2020; Snæbjörnsdóttir et al., 2020; White et al., 2020).

The wide range in predicted field length scales is strongly controlled by the range of reaction rate constants and hydraulic conductivities, which are some of the principle

487 unknowns in any carbonization operation. Hydraulic conductivity can be constrained
 488 by careful aquifer characterization, but the *in-situ* value of k is more challenging to char-
 489 acterize. By contrast, the process length is obviously a known and the relative concen-
 490 tration at the exit well Γ_{ex} , can be readily measured. Thus, there is an opportunity to
 491 use our scaling in an ‘inverse’ sense to obtain an estimate of the ‘effective’ *in-situ* rate
 492 constant. This is accomplished by rewriting eq. (31) as

$$493 \quad k = \frac{\ell_p^2 K_i \Delta h}{L_p^2}, \quad (44)$$

494 which only requires an estimation of the length over which precipitation is occurring (defin-
 495 ing both L_p and ℓ_p), in addition to the hydraulic parameters of the aquifer that are gen-
 496 erally easier to estimate than k . For example, the CarbFix 1 injection had an approx-
 497 imate well separation of 125 m between the injection well and monitoring well where sig-
 498 nificant carbon removal had been observed (Snæbjörnsdóttir et al., 2018, 2017). They
 499 also characterized the horizontal permeability to be $3 \times 10^{-13} \text{ m}^2$, which, for water, gives
 500 a hydraulic conductivity around $3 \times 10^{-6} \text{ [m/s]}$. Given the fact some dissolution occurred
 501 in that system, a reasonable range of L_p is 25 to 100 m. When used with the other pa-
 502 rameters values in eq. (42) and eq. (32) this reduces the possible range on the reaction
 503 rate by almost 3 orders of magnitude

$$504 \quad 1 \times 10^{-7} < k < 2 \times 10^{-5} [1/\text{s}].$$

505 The point here is that with a given operating condition and the knowledge of hydraulic
 506 conductivity in the domain, this proposed scaling can be used to impose significant con-
 507 straints on the effective first-order reaction rate constant.

508 **5.3 Shut-off time**

509 With a better constrained estimate of the effective reaction rate, we can use eq.(36)
 510 to improve the bounds on the time for shutoff. Presuming $\phi_i = 0.1$, $Y = 0.001$, and
 511 using the estimated values of k in eq.(5.2), the dimensional shutoff time falls in the range

$$512 \quad 50 \text{ days} < t_{\text{off}} < 30 \text{ years}$$

513 Returning to information from the CarbFix 1 site, we note that injection ran for approx-
 514 imately 90 days with no reported signs of clogging due to stored carbon (Snæbjörnsdóttir
 515 et al., 2020), suggesting that our analysis provides a meaningful time range.

516 **6 Conclusions**

517 By considering a simple model of mineral precipitation in a 1D porous media, we
 518 have developed a first-order model which represents the key processes relevant to car-
 519 bon mineralization. By considering a dimensional analysis of this model, we have fur-
 520 ther identified the key length and time scales of the operation. These are specifically, the
 521 length of the domain where mineralization occurs,

$$522 \quad L_p = \sqrt{|\ln(\Gamma_{ex})| + |\ln(\Gamma_{ex})|^2 \frac{\beta_L}{\phi_i}} \sqrt{\frac{K_i \Delta h}{k}}$$

523 and the time when clogging shuts off fluid flow,

$$524 \quad t_{\text{off}} = \frac{\phi_i}{\nu_S C_0 k},$$

525 both of which depend on intrinsic aquifer properties and the operational parameters of
 526 the mineralization operation. These scales are necessary first steps to evaluate the to-
 527 tal capacity of an aquifer and the time needed to realize that capacity. The scalings pro-
 528 vide not only a sense for the required sizes and operation times of a mineralization op-
 529 eration, but we have also shown that they can be used to place tighter constraints on

530 poorly constrained parameters, especially the effective first-order reaction rate constant

$$531 \quad k = \frac{\ell_p^2 K_i \Delta h}{L_p^2},$$

532 a vital, but poorly constrained parameter. Finally, the scales identified also confirm the
 533 critical characteristics that make for ideal mineralization: sufficient aquifer conductiv-
 534 ity to allow injected CO₂ to access the target formation, moderate reactivity such that
 535 mineralization occurs quickly without rapid clogging, and sufficient pore space such that
 536 meaningful amounts of carbon can be stored. In light of those aquifer characteristics, the
 537 scalings suggest parameters that can be controlled (e.g., injection head and reactant con-
 538 centrations) to engineer a desired domain size (length) and process time for a mineral-
 539 ization operation. This study provides a powerful tool for understanding and optimiz-
 540 ing *in-situ* carbon mineralization.

541 Open Research Section

542 The main data in this paper is developed from theoretical considerations, and no
 543 additional data is required to interpret or reproduce the work here. Any cited data, in-
 544 cluding parameter values derived in the supplementary information, was derived solely
 545 from the referenced values from the literature.

546 Acknowledgments

547 This work was supported as part of the Center on Geo-process in Mineral Carbon Stor-
 548 age, an Energy Frontier Research Center funded by the U.S. Department of Energy, Of-
 549 fice of Science, Basic Energy Sciences at the University of Minnesota under award # DE-
 550 SC0023429.

551 References

- 552 Anovitz, L. M., Beckingham, L. E., Sheets, J. M., & Cole, D. R. (2022, February).
 553 A Quantitative Approach to the Analysis of Reactive Mineralogy and Surface
 554 Area. *ACS Earth and Space Chemistry*, *6*(2), 272–287. (Publisher: American
 555 Chemical Society) doi: 10.1021/acsearthspacechem.1c00198
- 556 Arvidson, R. S., Ertan, I. E., Amonette, J. E., & Luttge, A. (2003, May). Varia-
 557 tion in calcite dissolution rates: A fundamental problem? *Geochimica et Cos-
 558 mochimica Acta*, *67*(9), 1623–1634. doi: 10.1016/S0016-7037(02)01177-8
- 559 Awolayo, A. N., Laureijs, C. T., Byng, J., Luhmann, A. J., Lauer, R., & Tutolo,
 560 B. M. (2022, October). Mineral surface area accessibility and sensitivity
 561 constraints on carbon mineralization in basaltic aquifers. *Geochimica et Cos-
 562 mochimica Acta*, *334*, 293–315. doi: 10.1016/j.gca.2022.08.011
- 563 Bear, J. (1972). *Dynamics of Fluids in Porous Media*. Dover.
- 564 Callow, B., Falcon-Suarez, I., Ahmed, S., & Matter, J. (2018, March). Assessing
 565 the carbon sequestration potential of basalt using X-ray micro-CT and rock
 566 mechanics. *International Journal of Greenhouse Gas Control*, *70*, 146–156.
 567 doi: 10.1016/j.ijggc.2017.12.008
- 568 Carman, P. C. (1997, December). Fluid flow through granular beds. *Chemical Engi-
 569 neering Research and Design*, *75*, S32–S48. doi: 10.1016/S0263-8762(97)80003-
 570 2
- 571 Clark, D. E., Oelkers, E. H., Gunnarsson, I., Sigfússon, B., Snæbjörnsdóttir, S. Ó.,
 572 Aradóttir, E. S., & Gíslason, S. R. (2020, June). CarbFix2: CO₂ and H₂S
 573 mineralization during 3.5 years of continuous injection into basaltic rocks
 574 at more than 250 °C. *Geochimica et Cosmochimica Acta*, *279*, 45–66. doi:
 575 10.1016/j.gca.2020.03.039

- 576 Gelhar, L. W., Welty, C., & Rehfeldt, K. R. (1992). A critical review of data on
577 field-scale dispersion in aquifers. *Water Resources Research*, *28*(7), 1955–1974.
578 doi: 10.1029/92WR00607
- 579 Gouze, P., & Luquot, L. (2011). X-ray microtomography characterization of poros-
580 ity, permeability and reactive surface changes during dissolution. *Journal of*
581 *Contaminant Hydrology*, *120-121*, 45–55. doi: 10.1016/j.jconhyd.2010.07.004
- 582 Gouze, P., Noiriél, C., Bruderer, C., Loggia, D., & Leprovost, R. (2003). X-ray
583 tomography characterization of fracture surfaces during dissolution. *Geo-*
584 *physical Research Letters*, *30*(5). Retrieved 2020-03-10, from [https://](https://agupubs.onlinelibrary.wiley.com/doi/abs/10.1029/2002GL016755)
585 agupubs.onlinelibrary.wiley.com/doi/abs/10.1029/2002GL016755 doi:
586 10.1029/2002GL016755
- 587 Gysi, A. P., & Stefánsson, A. (2011, September). CO₂-water-basalt inter-
588 action. Numerical simulation of low temperature CO₂ sequestration into
589 basalts. *Geochimica et Cosmochimica Acta*, *75*(17), 4728–4751. doi:
590 10.1016/j.gca.2011.05.037
- 591 Helgeson, H. C., Murphy, W. M., & Aagaard, P. (1984, December). Thermody-
592 namic and kinetic constraints on reaction rates among minerals and aque-
593 ous solutions. II. Rate constants, effective surface area, and the hydrolysis
594 of feldspar. *Geochimica et Cosmochimica Acta*, *48*(12), 2405–2432. doi:
595 10.1016/0016-7037(84)90294-1
- 596 Kang, P. K., Bresciani, E., An, S., & Lee, S. (2019, January). Potential impact of
597 pore-scale incomplete mixing on biodegradation in aquifers: From batch exper-
598 iment to field-scale modeling. *Advances in Water Resources*, *123*, 1–11. doi:
599 10.1016/j.advwatres.2018.10.026
- 600 Kelemen, P. B., McQueen, N., Wilcox, J., Renforth, P., Dipple, G., & Vankeuren,
601 A. P. (2020, September). Engineered carbon mineralization in ultramafic rocks
602 for CO₂ removal from air: Review and new insights. *Chemical Geology*, *550*,
603 119628. doi: 10.1016/j.chemgeo.2020.119628
- 604 Kozeny, J. (1927, April). Ueber kapillare Leitung des Wassers im Boden. *Sitzungs-*
605 *berichte Akademie der Wissenschaften in Wien*, *126*(2a), 271–306.
- 606 Lasaga, A. C. (1995, January). Fundamental approaches in describing mineral disso-
607 lution and precipitation rates. *Reviews in Mineralogy and Geochemistry*, *31*(1),
608 23–86.
- 609 Lasaga, A. C. (1997). *Kinetic Theory in the Earth Sciences* (1st ed.). Princeton Uni-
610 versity Press.
- 611 Lin, Y.-P., & Singer, P. C. (2005, September). Effects of seed material and solu-
612 tion composition on calcite precipitation. *Geochimica et Cosmochimica Acta*,
613 *69*(18), 4495–4504. doi: 10.1016/j.gca.2005.06.002
- 614 Matter, J. M., Stute, M., Snæbjörnsdóttir, S. Ó., Oelkers, E. H., Gislason, S. R.,
615 Aradottir, E. S., . . . Broecker, W. S. (2016, June). Rapid carbon miner-
616 alization for permanent disposal of anthropogenic carbon dioxide emissions.
617 *Science*, *352*(6291), 1312–1314. doi: 10.1126/science.aad8132
- 618 Morse, J. W., Arvidson, R. S., & Lüttge, A. (2007, February). Calcium Carbonate
619 Formation and Dissolution. *Chemical Reviews*, *107*(2), 342–381. doi: 10.1021/
620 cr050358j
- 621 Nancollas, G. H., & Reddy, M. M. (1971, December). The crystallization of calcium
622 carbonate. II. Calcite growth mechanism. *Journal of Colloid and Interface Sci-*
623 *ence*, *37*(4), 824–830. doi: 10.1016/0021-9797(71)90363-8
- 624 Noiriél, C., Luquot, L., Madé, B., Raimbault, L., Gouze, P., & van der Lee, J. (2009,
625 July). Changes in reactive surface area during limestone dissolution: An exper-
626 imental and modelling study. *Chemical Geology*, *265*(1), 160–170. doi: 10
627 .1016/j.chemgeo.2009.01.032
- 628 Parkhurst, D., & Appelo, C. (2013). Description of Input and Examples for
629 PHREEQC Version 3 — A Computer Program for Speciation , Batch-Reaction
630 , One-Dimensional Transport , and Inverse Geochemical Calculations. In

- 631 *book 6, ch. a43* (p. 497). United States Geological Survey. (available only at
632 [https://pubs.usgs.gov/tm/06/a43/.](https://pubs.usgs.gov/tm/06/a43/))
- 633 Plummer, L. N., Parkhurst, D. L., & Wigley, T. M. L. (1979, March). Critical Re-
634 view of the Kinetics of Calcite Dissolution and Precipitation. In E. A. Jenne
635 (Ed.), *Chemical Modeling in Aqueous Systems* (Vol. 93, pp. 537–573). WASH-
636 INGTON, D. C.: AMERICAN CHEMICAL SOCIETY. doi: 10.1021/bk-1979
637 -0093.ch025
- 638 Plummer, L. N., Wigley, T. M. L., & Parkhurst, D. L. (1978, February). The kine-
639 tics of calcite dissolution in CO₂-water systems at 5 degrees to 60 degrees C
640 and 0.0 to 1.0 atm CO₂. *American Journal of Science*, 278(2), 179–216. doi:
641 10.2475/ajs.278.2.179
- 642 Power, I. M., Harrison, A. L., Dipple, G. M., Wilson, S., Kelemen, P. B., Hitch,
643 M., & Southam, G. (2013, January). Carbon Mineralization: From Natural
644 Analogues to Engineered Systems. *Reviews in Mineralogy and Geochemistry*,
645 77(1), 305–360. doi: 10.2138/rmg.2013.77.9
- 646 Reddy, M. M., & Nancollas, G. H. (1971, June). The crystallization of calcium car-
647 bonate: I. Isotopic exchange and kinetics. *Journal of Colloid and Interface Sci-*
648 *ence*, 36(2), 166–172. doi: 10.1016/0021-9797(71)90161-5
- 649 Reddy, M. M., & Nancollas, G. H. (1976, August). The crystallization of calcium
650 carbonate: IV. The effect of magnesium, strontium and sulfate ions. *Journal of*
651 *Crystal Growth*, 35(1), 33–38. doi: 10.1016/0022-0248(76)90240-2
- 652 Saar, M. O., & Manga, M. (1999). Permeability-porosity relationship in
653 vesicular basalts. *Geophysical Research Letters*, 26(1), 111–114. doi:
654 10.1029/1998GL900256
- 655 Sabo, M. S., & Beckingham, L. E. (2021). Porosity-Permeability Evolution Dur-
656 ing Simultaneous Mineral Dissolution and Precipitation. *Water Resources Re-*
657 *search*, 57(6), e2020WR029072. doi: 10.1029/2020WR029072
- 658 Snæbjörnsdóttir, S. Ó., Gislason, S. R., Galeczka, I. M., & Oelkers, E. H. (2018,
659 January). Reaction path modelling of in-situ mineralisation of CO₂ at the
660 CarbFix site at Hellisheidi, SW-Iceland. *Geochimica et Cosmochimica Acta*,
661 220, 348–366. doi: 10.1016/j.gca.2017.09.053
- 662 Snæbjörnsdóttir, S. Ó., Oelkers, E. H., Mesfin, K., Aradóttir, E. S., Dideriksen, K.,
663 Gunnarsson, I., . . . Gislason, S. R. (2017, March). The chemistry and satu-
664 ration states of subsurface fluids during the in situ mineralisation of CO₂ and
665 H₂S at the CarbFix site in SW-Iceland. *International Journal of Greenhouse*
666 *Gas Control*, 58, 87–102. doi: 10.1016/j.ijggc.2017.01.007
- 667 Snæbjörnsdóttir, S. Ó., Sigfússon, B., Marieni, C., Goldberg, D., Gislason, S. R.,
668 & Oelkers, E. H. (2020, February). Carbon dioxide storage through min-
669 eral carbonation. *Nature Reviews Earth & Environment*, 1(2), 90–102. doi:
670 10.1038/s43017-019-0011-8
- 671 Viswanathan, H. S., Ajo-Franklin, J., Birkholzer, J. T., Carey, J. W., Guglielmi, Y.,
672 Hyman, J. D., . . . Tartakovsky, D. M. (2022). From Fluid Flow to Coupled
673 Processes in Fractured Rock: Recent Advances and New Frontiers. *Reviews of*
674 *Geophysics*, 60(1), e2021RG000744. doi: 10.1029/2021RG000744
- 675 White, S. K., Spane, F. A., Schaef, H. T., Miller, Q. R. S., White, M. D., Horner,
676 J. A., & McGrail, B. P. (2020, November). Quantification of CO₂ Mineral-
677 ization at the Wallula Basalt Pilot Project. *Environmental Science & Tech-*
678 *nology*, 54(22), 14609–14616. (Publisher: American Chemical Society) doi:
679 10.1021/acs.est.0c05142